

ICES REPORT 18-11

May 2018

Calibration of Multi-Parameter Models of Avascular Tumor Growth Using Time Resolved Microscopy Data

by

E.A.B.F. Lima, A. Ozkan, N. Ghousifam, J.T. Oden, A. Shahmoradi, M.N. Rylander, B. Wohlmuth, and
T.E. Yankeelov



The Institute for Computational Engineering and Sciences
The University of Texas at Austin
Austin, Texas 78712

Reference: E.A.B.F. Lima, A. Ozkan, N. Ghousifam, J.T. Oden, A. Shahmoradi, M.N. Rylander, B. Wohlmuth, and T.E. Yankeelov, "Calibration of Multi-Parameter Models of Avascular Tumor Growth Using Time Resolved Microscopy Data," ICES REPORT 18-11, The Institute for Computational Engineering and Sciences, The University of Texas at Austin, May 2018.

Calibration of Multi-Parameter Models of Avascular Tumor Growth Using Time Resolved Microscopy Data

E. A. B. F. Lima^{1,*}, A. Ozkan², N. Ghausifam², J. T. Oden¹, A. Shahmoradi^{3,4}, M. N. Rylander^{2,3}, B. Wohlmuth⁵, and T. E. Yankeelov^{1,3,6,7,8}

¹Institute for Computational Engineering and Sciences, The University of Texas at Austin, Austin, 78712, USA

²Department of Mechanical Engineering, The University of Texas at Austin, Austin, 78712, USA

³Department of Biomedical Engineering, The University of Texas at Austin, Austin, 78712, USA

⁴Department of Neurology, Dell Medical School, The University of Texas at Austin, Austin, 78712, USA

⁵Department of Mathematics, Technical University of Munich, Garching, 85748, Germany

⁶Department of Diagnostic Medicine, The University of Texas at Austin, Austin, 78712, USA

⁷Department of Oncology, The University of Texas at Austin, Austin, 78712, USA

⁸Livestrong Cancer Institutes, Dell Medical School, The University of Texas at Austin, Austin, 78712, USA

*lima@ices.utexas.edu

ABSTRACT

One of the central challenges when using tumor growth models for predicting the spatiotemporal development of tumors is the lack of appropriate data to calibrate the parameters of the model. In this work, we present a sequence of experiments, with increasing complexity, designed to systematically calibrate the rates of apoptosis, proliferation, and necrosis, as well as mobility, within a phase-field tumor growth model. The *in vitro* experiments characterize the proliferation and death of human liver carcinoma cells under different initial cell concentrations, nutrient availabilities, and treatment conditions. A Bayesian framework is employed to quantify the uncertainties in model parameters. The average difference between the calibration and the data, across all time points, for each experimental scenario, is between 7.33% and 31.55%. The calibration of the parameters indicates that the proposed set of experiments are adequate for the step-by-step calibration of the model. The difference between the calibration of the parameter at one scenario, and its update at a scenario with higher experimental complexity, is below 5%. The model is able to calibrate the tumor mobility, with an average Pearson correlation coefficient of 0.78.

Introduction

There has been increasing interest in the development and application of mathematical models to describe the initiation, growth, and response of tumors to treatment^{1,2}. These models are frequently used to calibrate against experimental data to estimate model parameters which can then be used (for example) to predict the spatiotemporal evolution of tumors. The process of model calibration requires that a sequence of experiments be designed in which one or more dependent variables are fully prescribed or are held constant while others are allowed to vary, and parameters are assigned so as to fit model predictions with experimental observations³⁻¹¹. Two areas of excitement within the field are related to 1) the increasing interplay between experiment and theory, and 2) characterizing the experimental and computational uncertainties inherent in such efforts. The limited progress in these areas, historically, has prevented mathematical oncology from reaching its promise, the result is that, the modeling can, at best, produce only qualitative descriptions of tumor growth and cannot generally be used as a basis for predicting, with precision, the outcomes of various therapies. In the present effort, we address both of these limitations by designing a set of *in vitro* studies which were designed to systematically provide inputs for the mathematical model via serial microscopy measurements.

The capability of computational models to accurately predict the complex and dynamic nature of tumor progression, intrinsic intra-tumoral heterogeneity, and spatial aspects of tumor cell migration requires acquisition of experimentally measured parameters which capture these phenomena with sufficient spatial and temporal resolution. Serial microscopy measurements provide a convenient system in which to address this issue as both high spatial and temporal data can be acquired over a sufficiently large field-of-view to enable characterization of biological heterogeneity. There has been some previous effort, with varying levels of complexity, in mathematical formulation and experimental parameter estimation

for the system of interest. In particular, some efforts have focused on modeling a homogenous tumor with emphasis on prediction of the time dependent response to therapy¹². For example McKenna *et al.* developed and experimentally validated a coupled pharmacokinetic/pharmacodynamics model to predict the temporal response of a homogeneous cell population to a temporally-varying treatment time course. For this study, longitudinal fluorescence microscopy experiments were used to characterize the dynamics of doxorubicin uptake and population response to this drug in a variety of triple negative breast cancer cells lines¹². To capture the intrinsic heterogeneity of tumors, McKenna *et al.* expanded upon their prior coupled pharmacokinetics/pharmacodynamics model to determine the impact of cell population heterogeneity on therapy response to doxorubicin. For this work, characterization of the proliferation and death rates of each parental and drug resistant cell line within co-cultures were imaged and quantified dynamically using fluorescence microscopy to provide experimental inputs for the model¹³. Although the populations of proliferative and dead cells were quantified, neither hypoxic or apoptotic populations were determined. Waclaw *et al.* have modeled the influence of intra-tumor heterogeneity consisting of hepatocellular carcinoma using neoplastic and non-neoplastic cells on the spatial growth and resistance to therapeutic agents. Histopathology and microscopy were utilized to determine heterogeneous cell populations from human biopsies and this information provided critical input data for model formulation¹⁴. Tyson *et al.* have modeled single cell proliferation and drug response of lung cancer cells. For these studies, immunofluorescence labeling and time-lapse automated microscopy were used to calibrate their model to estimate single cell lifespan¹⁵. There is a significant need to extend these results through systematic integration of experimental data and modeling, and to quantify the uncertainties inherent in such studies.

Mathematical models which represent physical phenomena are subject to the inherent uncertainties in both the experimental data and the models themselves. Experimental data can be corrupted by both random and systemic error which leads to uncertainty when using these data to populate and calibrate model parameters, determine domain geometry, and setting initial conditions. The mathematical models contribute uncertainty through inadequacies in their underlying biological and physical assumptions, and implementation of the boundary conditions. If such uncertainties are not accounted for, the model will provide predictions that are biased to an extent determined by those uncertainties. In the case of tumor modeling, these errors may lead to predictions that mischaracterize the location and extent of disease, and intra-tumoral heterogeneity. We have developed a general framework for handling these uncertainties based on Bayesian theory^{16,17}. Briefly, observational data are collected and given a prior probability density on the model parameters from which we compute the posterior probability density (i.e., the calibration step). Then using the posterior probability density as a prior, we update the parameters (i.e., the validation step). The updated parameters are then used to solve the forward problem to determine prediction accuracy using an appropriate metric. Using this Bayesian approach, the parameters, the data, and even the model are not assumed to be deterministic; rather, they are considered as random variables characterized by probability density functions. These characterizations lead to a stochastic model that is able to propagate uncertainty from model inputs to outputs.

In this study, we describe a general approach for the Bayesian calibration of phenomenological models of avascular tumor growth that accounts for uncertainties in observational data, in model parameters, inadequacies of the model itself, and in the prediction of principal quantities of interest (e.g., the growth or decline of the tumor over time). We use this methodology to provide a general approach for the calibration of multi-parameter models to time-resolved (*in vitro*) microscopy data in which the proliferation and death of cell colonies are controlled and measured for prescribed levels of available nutrients, and in which specific experimental protocols are designed to control, isolate, and monitor the evolution of (in this case) liver cancer cells. The design of an integrated experimental-computational framework, and the determination of uncertainties in model parameters are the main contributions of this work.

Following this introduction, we provide a brief review to a large class of phenomenological tumor growth models based on a combination of biological models of cell proliferation, hypoxia, necrosis, and balance laws of continuum mixture theory. These classes include reaction-diffusion models, phase-field models, and models which account for mechanical deformation effects on cell mobility. To characterize uncertainties in the observable data, in model selection, as well as in the stochastic nature of the tumor growth and the model parameters, we call upon Bayesian statistical calibration procedures. Here Markov Chain Monte-Carlo sampling methods are used to calculate the posterior probability densities of key model parameters. We then provide the experimental details, allowing for model calibration of cell proliferation, cell death mechanisms, and mobility, as well as the influence of various concentrations of nutrient, and therapeutic agents. Finally, we provide detailed accounts of the statistical calibration of the *in vitro* experiments, and present probabilistic characterization of the key parameters.

Materials and Methods

Classes of phenomenological models of tumor growth

The class of tumor growth models considered here is an extension of the avascular model developed in^{16,17} in which we incorporate different phenotypes. The derivation of the full 10-field multispecies tumor growth model, characterized by a system of nonlinear, coupled, stochastic partial differential equations, is given in³. Here, we consider an open bounded region $\Omega \subset \mathbb{R}^3$, with smooth boundary, $\partial\Omega$, which contains an evolving and interacting mass of tumor cells concentrations of which

are represented by scalar-valued functions of position $x \in \Omega$ and time $t \in [0, T]$, representing the volume fraction of each tumor cell species. The volume fraction of tumor cells at x at time t is denoted by $\phi_T(x, t)$, while that of proliferative, hypoxic, and necrotic cells is denoted $\phi_P(x, t)$, $\phi_H(x, t)$ and $\phi_N(x, t)$, respectively. To align the model complexity with experimental data, we denote the viable and tumor cells volume fraction by

$$\left. \begin{aligned} \phi_V(x, t) &= \phi_P(x, t) + \phi_H(x, t), \\ \phi_T(x, t) &= \phi_V(x, t) + \phi_N(x, t). \end{aligned} \right\} \quad (1)$$

In general, the mass-balance equations for the mixture take the form,

$$\frac{\partial \rho_\alpha \phi_\alpha}{\partial t} + \nabla \cdot (\rho_\alpha \phi_\alpha v_\alpha) = \rho_\alpha (\nabla \cdot J_\alpha + S_\alpha), \quad (2)$$

where v_α is the local convection velocity of species α , $\rho_\alpha J_\alpha$ is the mass flux, $\rho_\alpha S_\alpha$ is the mass supplied constituent α by other constituents, $\nabla = \sum_i \frac{\partial}{\partial x_i}$ is the spatial gradient operator. A common assumption, and one invoked here, is that the mass densities ρ_α of all constituents are essentially the same $\rho_\alpha = \rho_C = \text{one constant}$ ^{6,7,16–19}. Assuming that the evolution of tumor growth generally takes place over a relatively long time intervals, the convective velocity v_α can be set to zero, leaving the reduced form of mass balance,

$$\frac{\partial \phi_\alpha}{\partial t} = \nabla \cdot J_\alpha + S_\alpha, \quad \alpha = T, V, N. \quad (3)$$

Various biological events (cell mitosis and proliferation, apoptosis, hypoxia, etc.) are modeled through fluxes and sources (i.e., J_α and S_α , respectively) designed to follow rules inspired by well-known hallmarks of cancer cell biology. The mass flux J_α depends linearly on the gradient of the chemical potential μ , according to

$$J_\alpha = -M_\alpha(\phi) \nabla \mu, \quad (4)$$

where $M_\alpha(\phi)$ is the positive-semi-definite mobility matrix for species α , possibly dependent on species ϕ , $\phi = \{\phi_T, \phi_V, \phi_N\}$.

The segregation and adhesion properties among the mixture constituents are modeled by a free energy functional (E) that sums the contribution of the α^{th} constituent, E_α , to the total energy; that is, $E = \sum_{\alpha=1}^N E_\alpha$. We assume that tumor cells prefer to adhere to each other⁽¹⁹⁾ so that they remain segregated, forming clusters of tumor cells, and conform to a double-well form of bulk energy, $\Psi(\phi_T)$. The double-well function is zero at the pure phases, $\phi_T = 0$ and $\phi_T = 1$, driving the segregation into the pure phases. We also assume, for simplicity, that the adhesive properties of all tumor cells (viable and necrotic) are similar. As the adhesion between the cells increases, the length of the interface, ε_T , between the pure phases decreases. These assumptions yield the following total energy of the system:

$$E = \int_{\Omega} \left[\Psi(\phi_T) + \frac{\varepsilon_T^2}{2} |\nabla \phi_T|^2 \right] dx, \quad (5)$$

where ε_T is the interaction length (i.e., the boundary-layer thickness between phases), and $\Psi(\phi)$ is defined by a quartic double-well potential. The double-well potential is assumed to be of the polynomial form,

$$\Psi(\phi_T) = \bar{E}_T \phi_T^2 (1 - \phi_T)^2, \quad (6)$$

where $\bar{E}_T > 0$ is the energy scale associated with the tumor volume fraction. The free-energy can be decomposed into contractive and expansive terms⁽²⁰⁾,

$$\Psi(\phi) = \bar{E}_T \phi_T^2 (1 - \phi_T)^2 = \Psi_c(\phi_T) - \Psi_e(\phi_T), \quad (7)$$

where

$$\Psi_c(\phi_T) = \frac{3}{2} \bar{E}_T \phi_T^2, \quad \Psi_e(\phi_T) = -\bar{E}_T \left(\phi_T^4 - 2\phi_T^3 - \frac{1}{2}\phi_T^2 \right). \quad (8)$$

Such splitting, though not unique, always exists for each form of the energy functional and it provides a basis for developing unconditionally stable numerical schemes to advance the evolution of each cell species in time.

From arguments on the thermodynamics of the mixture (e.g.,^{9,10}), it can be inferred that the chemical potential is the partial Gateaux derivative of the total free energy E , with respect to the tumor volume fraction, ϕ_T . Thus, for E given by Eq. (5),

$$\mu = \Psi'(\phi_T) - \varepsilon_T^2 \Delta \phi_T. \quad (9)$$

The mass source terms S_α in Eq. (3) are designed to capture various states of cell viability that depend on nutrient supply and cell concentrations. With the notion that the local dynamics of the tumor growth depend on the nutrient availability, σ_{VN} is introduced as the nutrient threshold which determines the transfer from viable to necrotic cell states. The viable tumor cells can grow until reaching the carrying capacity, K , when consuming nutrient with a constant rate of cellular mitosis, λ_{prol} . They also decay owing to natural death of cells at the apoptosis rate, λ_{apop} . Moreover, when the level of nutrient drops below σ_{VN} , the viable cells become part of the necrotic core at the rate, λ_{VN} . We assume that the necrotic core of the tumor never decreases. With these assumptions, the source terms in our model take the following forms:

$$\begin{aligned} S_V &= \lambda_{prol} \phi_\sigma \phi_V \left(1 - \frac{\phi_V + \phi_N}{K} \right) - \lambda_{apop} \phi_V - \lambda_{VN} \mathcal{H}(\sigma_{VN} - \phi_\sigma) \phi_V, \\ S_N &= \lambda_{VN} \mathcal{H}(\sigma_{VN} - \phi_\sigma) \phi_V, \end{aligned}$$

where \mathcal{H} is the Heaviside step function ($\mathcal{H}(x) = 0, x < 0, \mathcal{H}(x) = 1, x \geq 0$).

In light of the above arguments, assumptions, and approximations, the governing equations are

$$\left. \begin{aligned} \frac{\partial \phi_T}{\partial t} &= \nabla \cdot \overline{M_T(\phi)} \nabla \mu + \overline{\lambda_{prol}} \phi_\sigma \phi_T \left(1 - \frac{\phi_T}{K} \right) - \overline{\lambda_{apop}} \phi_T \\ \mu &= \overline{\Psi'(\phi_T)} - \overline{\varepsilon_T}^2 \Delta \phi_T \\ \frac{\partial \phi_N}{\partial t} &= \nabla \cdot \overline{M_N(\phi)} \nabla \mu + \overline{\lambda_{VN}} \mathcal{H}(\overline{\sigma_{VN}} - \phi_\sigma) (\phi_T - \phi_N) \end{aligned} \right\} \quad (10)$$

Thus, nine model parameters remain to be determined or calibrated (highlighted in Eq. (10)). To solve these equations, appropriate boundary and initial conditions are required and we take zero flux boundary conditions on ϕ_T , ϕ_N , and μ (see e.g., ^{6,16,17}):

$$\nabla \phi_T \cdot n = 0, \quad \nabla \phi_N \cdot n = 0, \quad \nabla \mu \cdot n = 0, \quad \text{on } \partial\Omega \times (0, T), \quad (11)$$

where n is normal to $\partial\Omega$. The initial conditions $0 \leq \phi_{T0}(x) \leq 1$ and $0 \leq \phi_{N0}(x) \leq 1, \forall x \in \Omega$, are measured directly by the experiments described below.

Bayesian statistical calibration

Bayesian inversion provides a comprehensive and consistent framework for statistical calibration of model parameters which accounts for uncertainties in both observational data and in model selection, as well as delivering consistent probabilistic representations of model parameters^{3,17,21}. We now summarize the key features of Bayesian parameter estimation.

Let $A : \Theta \times U \rightarrow V$ denote the operators defining the model of interest, U and V being appropriate function spaces, and let the abstract problem of finding $\phi \in U$ such that,

$$A(\theta, \phi) = 0, \quad (12)$$

be the *forward problem*, $\theta \in \Theta$ being a vector of model parameters taken from a parameter space Θ . For the problem described by Eq. (12), $\theta = \{M_T, M_N, \lambda_{prol}, K, \lambda_{apop}, \bar{E}_T, \varepsilon_T, \lambda_{VN}, \sigma_{VN}\}^T$,

$$A = \left\{ \begin{array}{l} \frac{\partial \phi_T}{\partial t} \\ \mu \\ \frac{\partial \phi_N}{\partial t} \end{array} \right. - B(U), \quad (13)$$

$U = \{\phi_T, \mu, \phi_N\}^T$, with $B(\cdot)$ the right-hand-side, and with the understanding that nutrient volume fraction ϕ_σ will be prescribed as data. The goal is to choose the parameters θ so that the model (12) agrees with a physical reality of interest denoted as g . Of course, such realities cannot be realized exactly; they are only available to use via experimental data y which is always corrupted by experimental noise.

Since the dependent variables in our model are volume fractions of different tumor cell phenotypes, and since the key quantities of interest could be chosen to be the viable tumor volume at times $t_i \in [0, T_{end}]$, $i = 1, 2, \dots, n$, the physical realities of interest are $g_i = \mathbb{E}[\int_\Omega \phi_V(x, t_i) dx]$, with $\phi_V = \phi_T - \phi_N$. Thus, we will need an experimental approach that allows the measurement of ϕ_V at specified time intervals. The observational data $y = \{y_i\}_{i=1}^n$ must, in these scenarios, consist of measurements of cell concentrations (or volume fractions) at these times given specified nutrient concentrations. (We describe in the next section the experimental procedure for measuring ϕ_V , given ϕ_σ .) The cell counts are actually estimated from fluorescence images (details

provided below). The conversion from florescence signal to cell numbers (and, hence, volume fraction) includes experimental error or noise. We shall employ as a model of experimental noise the additive relation

$$g_i = y_i + \varepsilon_i, \quad \varepsilon_i \sim \mathbb{P}_v, \quad (14)$$

g_i being the physical reality at test point i , y_i the observational data, and \mathbb{P}_v a probability model for ε_i with new hyperparameters (i.e., a parameter that is not part of the model under analysis) v . We employ a Gaussian noise model written as:

$$\mathbb{P}_v \sim \mathcal{N}(m, \sigma^2 I), \quad (15)$$

m being a mean, and σ^2 the variance.

Next we turn to the model prediction. For a sample $\theta \in \Theta$ of the model parameters drawn from the parameter space Θ , we solve the forward problem (i.e., Eq. (10) or its observation Eq. (12)) for $U(\theta; x, t)$ and compute the model predictions, denoted $d_i(\theta)$ of the data g_i . The difference between reality and prediction for each choice of θ is the model inadequacy $\eta_i(\theta)$. As in (14), we introduce a probabilistic model for model inadequacy:

$$\begin{cases} g_i = d_i(\theta) - \eta_i(\theta), & i = 1, 2, \dots, n, \\ \eta_i(\theta) \sim \mathbb{P}_\gamma \sim \mathcal{N}(\hat{m}, \hat{\sigma}^2 I), \end{cases} \quad (16)$$

where \hat{m} and $\hat{\sigma}^2$ are additional hyperparameters, and a Gaussian probability model is again employed. Subtracting Eq. (16) from Eq. (14) gives

$$\begin{cases} y_i - d_i(\theta) = \varepsilon_i + \eta_i(\theta), \\ \mathbb{P}_{v+\gamma} \sim \mathcal{N}(m, \sigma^2 I) + \mathcal{N}(\hat{m}, \hat{\sigma}^2 I). \end{cases} \quad (17)$$

If $\mathbb{P}_{v+\gamma}$ is the probability density of the combined noise-inadequacy model (17), the likelihood probability density $\pi(\cdot, \cdot)$ is the conditional density

$$\begin{cases} \pi(y_i|\theta) & = \mathbb{P}_{v+\gamma}(\varepsilon_i + \eta_i(\theta)), \\ & = \mathbb{P}_{v+\gamma}(y_i - d_i(\theta)), \end{cases} \quad (18)$$

where $i = 1, 2, \dots, n$.

Since a Bayesian calibration process is to be used, prior probability densities $\pi(\theta)$ on all parameters must be specified. When no prior information is known about a parameter θ_i , except bounds $\theta_i \in (a, b)$, we employ the uniform prior $\theta_i \sim \mathcal{U}(a, b)$. If mean and variance are known approximately, a Gaussian prior, or a truncated Gaussian, can be used. The Bayesian update in model parameters θ is furnished by the posterior probability density $\pi(\theta|y)$

$$\pi(\theta|y_i) = \frac{\pi(y_i|\theta)\pi(\theta)}{\pi(y_i)}, \quad (19)$$

where the denominator, called the model evidence, is the normalizing factor

$$\pi(y_i) = \int_{\Theta} \pi(y_i|\theta)\pi(\theta)d\theta. \quad (20)$$

Based on the assumptions of a Gaussian noise-inadequacy model and independent and identically distributed samples of experimental data, we then construct the likelihood function (18) as:

$$\pi(y|\theta) = \prod_{j=1}^{\mathcal{N}_t} \prod_{i=1}^{\mathcal{N}_r} \frac{1}{\sqrt{2\pi\sigma^2}} e^{-\frac{(y^{ij} - d_c^j(\theta))^2}{2\sigma^2}}, \quad (21)$$

where \mathcal{N}_t is the number of days measured, \mathcal{N}_r is the number of replicates per day, σ is an hyperparameter (the standard deviation for the Gaussian) related to the size of the noise, d_c is the volume fraction of viable cells predicted by the model, and y is the experimentally measured data against which the model is calibrated.

For the scenarios where the spatial distribution must be taken into account, such as the mobility calibration, the Pearson correlation coefficient (PCC) is computed to measure the linear correlation between the measured data and the calibrated model. The PCC has a value between 1 and -1, indicating total positive linear correlation or total negative linear correlation, respectively. A zero PCC indicates that there is no linear correlation between the two. We modify the likelihood function in Eq. (21) to take into account the PCC information. To maximize the linear correlation (i.e., PCC equals one), we construct the likelihood function as:

$$\pi(y|\theta) = \prod_{j=1}^{\mathcal{N}_t} \prod_{i=1}^{\mathcal{N}_r} \frac{1}{\sqrt{2\pi\sigma^2}} e^{-\frac{(1 - PCC(y^{ij} - d_c^j(\theta)))^2}{2\sigma^2}}. \quad (22)$$

In the next section we describe the experiments designed to provide the probability densities of the model parameters. The forward problem given by Eq. (10) is solved for M samples of the probability densities of each parameter in a Monte Carlo algorithm²².

Microscopy

Serial microscopy was performed using two different microscopes in this study. A BioTek plate reader (BioTek, Winooski, VT) was used to measure fluorescence of CellTiter-Blue assay with response to reaction with viable cells at every 24 hours. A Leica SP8 confocal microscope (Leica, Wetzlar, Germany) was used to capture the number and spatial distribution of cells within each well during each experiment described below. Each well was imaged at 30 minute intervals *via* fluorescence microscopy with a 10X dry objective in 1.16mm \times 1.16mm image montages with 2.275 μ m pixel size.

Cell culture preparation

Liver cancer, C3Asub28, cells were generously donated by Dr. Wei Li (The University of Texas at Austin) and cultured with DMEM/F12 (1:1) +L-Glutamine, +15mM HEPES (Invitrogen, CA) supplemented with 10% fetal bovine serum (FBS, Sigma Aldrich, MO) and 1% Penicillin/Streptomycin (Invitrogen, CA). Cells inside T-flasks were incubated (Thermo, MA) at 37°C, 95% atmospheric air (5% CO₂). Cell confluence was monitored every day and cells were used in experiments only when they were 70% confluent. The cells were then detached from the flasks and seeded to a 96-well plate (Corning Life Sciences, Cambridge, MA) with desired seeding density for further analysis. Samples were incubated at 37°C, 95% atmospheric air (5% CO₂) and media was replaced daily.

Determination of growth rate and cell viability

Cell viability was assessed using CellTiter-Blue® assay (Promega, WI) following the manufacturer's protocol. Viability of cells with 5 different initial seeding densities (5.0 \times 10³, 1.0 \times 10⁴, 2.5 \times 10⁴, 5.0 \times 10⁴, and 1.0 \times 10⁵ cells/ml) were tested every 24 hours for 21 days. Before applying the assay and measuring viable cell counts, cells were rinsed twice with phosphate-buffered saline (PBS, Sigma Aldrich, MO) to remove waste generated by the cells, which can affect the results of the assay due to increased acidity of the media.

Determination of apoptosis rate

To measure the viability of cells in the absence of proliferation, cell cultures were treated with Mitomycin C (MMC, Sigma Aldrich, MO). MMC is known as an inhibitor of cell proliferation^{23,24}. Cells were treated with 10 μ g/ml MMC for 120 minutes before detaching from the culture flask. After this treatment, MMC treated cancer cells were detached from culture flask and seeded with five different initial densities (5.0 \times 10³, 1.0 \times 10⁴, 2.5 \times 10⁴, 5.0 \times 10⁴, and 1.0 \times 10⁵ cells/ml) to 96 well plates. The viability protocol described in the previous section was conducted every 24 hours for 7 days. As the cell proliferation is inhibited, and the cells are in a nutrient-rich environment (i.e., 10% concentration of FBS), the only phenomena driving the change in the measured viability of cells is the apoptosis rate. These viability curves are used to calibrate the apoptosis rate from the model in Eq. (10).

Determination of growth rate with varying levels of nutrient concentration and necrosis rate

To investigate the effects of varying levels of nutrient concentration on the viability of cells, the concentration of FBS in the cell media was decreased from the usual concentration of 10% to 7.5%, 5%, 2.5% and 0% in a set of independent experiments. Four different initial cell concentrations were also utilized: 1.0 \times 10⁴, 2.5 \times 10⁴, 5.0 \times 10⁴, and 1.0 \times 10⁵ cells/ml to determine the impact on growth rate. Viability measurements were performed every 24 hours for 7 days. From the same set of samples, the cell death rate due to necrosis (primarily due to a lack of nutrient availability) can be also quantified. For the calibration of this scenario, the apoptosis rate is considered to be known from the previous experiments. Therefore, the increase in cell death is considered to be a consequence of cell starvation due to the change of FBS concentration. This parameter in Eq. (10), the necrosis rate (λ_{VN}), is calibrated using the viability curves measured with different FBS concentrations.

Determination of cell mobility with varying levels of nutrient concentration

Cell mobility in natural growth conditions were conducted by tracking each individual cell located in a 96 well plate. The C3Asub28 cells were transfected with green fluorescent protein (GFP) to label and allow for cell tracking. Cell locations were measured every 30 minutes for 12 hours for a initial seeding densities of 1.0 \times 10⁵ cells/ml, and 5 different nutrient concentrations (10%, 7.5%, 5%, 2.5% and 0%). The cells are segmented in MATLAB through a color-based segmentation using k-means clustering.

Conversion of fluorescence intensity measurements to cell number

The conversion of fluorescence intensity to cell number is essential to obtain estimates of the physical parameters included in the mathematical model. A proxy measure of cell volume fraction can be obtained by performing a linear correlation between

the initial cell count on day 0 with its fluorescence intensity. This allows for an estimation of the number of cells, $N_c(t)$, which can then be divided by the area of the well to compute the viable tumor cells volume fraction $\phi_V(t)$.

The resulting cell number versus time data is calibrated to each model described above to estimate model parameters. To assess the quality of the calibration, a metric using the cumulative probability distribution functions in $L^1(\mathbb{R})$ is proposed: Let $F_t(\phi_V)$ and $S_t(\phi_V)$ be the cumulative distribution functions for the model and the data at day t , respectively. The $L^1(\mathbb{R})$ metric for the data is then

$$d_t(F_t, S_t) = \frac{\int_0^\infty |F_t(\phi_V) - S_t(\phi_V)| d\phi_V}{\bar{y}_t}, \quad (23)$$

where \bar{y}_t is the mean tumor volume fraction from the data at time t . The simulations are computed on the Lonestar 5 Cluster, at the Texas Advanced Computing Center (TACC) of The University of Texas at Austin (URL: <http://www.tacc.utexas.edu>). The general purpose finite-element library `libMesh`²⁵, is used to compute the numerical solutions to the partial differential equations. The ordinary differential equations are solved using a fourth-order Runge-Kutta method. For model calibration, we employ a Parallel Tempering Monte Carlo algorithm (22) that is available in the library QUESO (Quantification of Uncertainty for Estimation, Simulation, and Optimization)²⁶.

Results

Calibration of apoptosis rates

To calibrate the apoptosis rate (λ_{apop}), we examine *in vitro* datasets of cell viability measured in the C3A liver cancer cell lines treated with Mitomycin-C (Figure 1a)). As we are only measuring the volume fraction of the viable tumor cells, initially without assessing the spatial distribution of the cells, and as the nutrient concentration is assumed to be sufficient to avoid hypoxia and necrosis, ϕ_T can be assumed to be equal to ϕ_V . With these assumptions, the model in Eq. (10) reduces to simply exponential death:

$$\frac{d\phi_V}{dt} = -\lambda_{apop}\phi_V, \quad (24)$$

where, the apoptosis rate (λ_{apop}), the initial tumor volume fraction (ϕ_{V0}), and the standard deviation (σ) hyperparameter from Eq. (21) are all calibrated. The calibration priors are assumed to be uniform distributions with $\lambda_{apop} \sim \mathcal{U}(0, 10)$, $\phi_{V0} \sim \mathcal{U}(10^{-5}, 1)$, and $\sigma \sim \mathcal{U}(10^{-5}, 20)$. The model is calibrated for the five initial cell concentration: 5.0×10^3 , 1.0×10^4 , 2.5×10^4 , 5.0×10^4 , and 1.0×10^5 cells/ml. The mean initial volume fractions, ϕ_{V0} , computed from the experiments are: 4.22×10^{-3} , 8.44×10^{-3} , 2.11×10^{-2} , 4.22×10^{-2} , and 8.44×10^{-2} , respectively.

In Figure 1a) we compare the calibration of the model with the *in vitro* experiments. Using the metric given in Eq. (23), the average error per initial condition (5,000 to 100,000 cells/ml) is 11.98%, 11.54%, 14.04%, 13.30%, and 12.59%, respectively. In Figure 2, the histogram of the apoptosis rate, λ_{apop} , for different initial conditions are presented. The results from the calibration indicates that the λ_{apop} is proportional to the initial concentration of cells, with the 5,000 and 10,000 cells/ml having the lowest ($\approx \mathcal{N}(0.06, 0.02)$), the 25,000 and 50,000 cells/ml the intermediate ($\approx \mathcal{N}(0.09, 0.03)$, and $\mathcal{N}(0.09, 0.02)$, respectively), and the 100,000 cells/ml the highest apoptosis rate ($\approx \mathcal{N}(0.11, 0.02)$). In Table 1, we summarize the fitted distributions for the parameters. It is possible to observe that this concentration of Mitomycin-C is enough to stop cell proliferation. This conclusion can be made by observing a 95% credible interval of the calibrated λ_{apop} at different initial condition: 0.06 ± 0.04 , 0.09 ± 0.06 , 0.09 ± 0.04 , and 0.11 ± 0.04 ; a negative apoptosis rate (or zero as our prior is positive) would indicate that the cells were proliferating.

Calibration of proliferation rates

To calibrate the proliferation rate (λ_{prol}), we use the dataset of cell volume fraction without Mitomycin-C (Figure 1b)). Similar to the apoptosis calibration, the model in Eq. (10) can be simplified to:

$$\frac{d\phi_V}{dt} = \lambda_{prol}\phi_\sigma\phi_V \left(1 - \frac{\phi_V}{K}\right) - \lambda_{apop}\phi_V, \quad (25)$$

where the proliferation rate (λ_{prol}), the carrying capacity (K), and the standard deviation (σ) hyperparameter from Eq. (21) are all calibrated. With this experiment, we update the distributions of the apoptosis rate (λ_{apop}) and the initial tumor volume fraction (ϕ_{V0}) during the calibration. The nutrient concentration is assumed to be sufficient to maximize the growth rate ($\phi_\sigma = 1$). The calibration priors are assumed to be uniform distributions with $\lambda_{prol} \sim \mathcal{U}(0, 10)$, $K \sim \mathcal{U}(0, 1)$, and $\sigma \sim \mathcal{U}(10^{-5}, 20)$, and the posteriors from the calibration using the data with Mitomycin-C are used as priors for ϕ_{V0} and λ_{apop} (i.e., the posteriors from Figure 2 are used as priors in this scenario).

In Figure 1b), the calibrated model and the *in vitro* data are compared. To assess the quality of the calibration, we compute the average error per initial condition *via* Eq. (23). The errors, from the lowest initial condition (5,000 cells/ml) to the highest (100,000 cells/ml), are 23.30%, 15.56%, 19.46%, 12.13%, and 7.33%, respectively. In Figure 3, we compare the prior and the posterior of the apoptosis rate. A metric similar to that in Eq. (23) is used with $F_t(\phi_V)$ and $S_t(\phi_V)$ now distribution functions for the posterior and the prior, and \bar{y} the mean value of λ_{apop} from the prior. The difference between the prior and posterior, per initial condition (5,000 to 100,000 cells/ml), on the calibration of the apoptosis rate, is 0.42%, 3.09%, 1.40%, 0.46%, and 4.38%, respectively. These small differences indicate that the calibration scenario for λ_{apop} , with Mitomycin-C, is in agreement with the scenario without Mitomycin-C, and can correctly calibrate the apoptosis rate. In Figure 4, the calibrated proliferation rates are presented. The approximated distributions for λ_{prol} , from the lowest initial condition to the highest, are $\approx \mathcal{N}(0.43, 0.02)$, $\approx \mathcal{N}(0.48, 0.02)$, $\approx \mathcal{N}(0.55, 0.05)$, $\approx \mathcal{N}(0.55, 0.05)$, and $\approx \ln \mathcal{N}(0.43, 0.64)$, respectively. The difference in the proliferation rate distribution for 100,000 cells/ml is due to the fact that, for this initial condition, the experiment starts with a volume fraction close to the carrying capacity of the well, as we can see in Figure 1b). After the third day, the volume fraction of tumor cells is not affected by the value of λ_{prol} , which explain the different distribution patterns.

Calibration of necrosis rates

The next experiment aims to calibrate the necrosis rate, λ_{VN} , using the data obtained from well provided with different nutrient concentrations (Figures 1c)-f)). In these experiments, the cell viability is measured for a series of nutrient concentrations that can lead to necrosis. With these assumptions, the model in Eq. (10) can be simplified to:

$$\left. \begin{aligned} \frac{d\phi_T}{dt} &= \lambda_{prol}\phi_\sigma\phi_T \left(1 - \frac{\phi_T}{K}\right) - \lambda_{apop}\phi_T, \\ \frac{d\phi_N}{dt} &= \lambda_{VN}(\phi_T - \phi_N). \end{aligned} \right\} \quad (26)$$

Note that in Eq. (26), we disregard the Heaviside function as we have observed that, for any concentration of nutrients below 10% of FBS, the condition $\sigma_{VN} - \phi_\sigma > 0$ holds. We calibrate the standard deviation (σ) hyperparameter from Eq. (21) and the necrosis rate (λ_{VN}), and update the distributions of the apoptosis rate (λ_{apop}), initial tumor volume fraction (ϕ_{V0}), proliferation rate (λ_{prol}), and carrying capacity (K). The calibration priors are assumed to be uniform distributions with $\lambda_{VN} \sim \mathcal{U}(0, 10)$, and $\sigma \sim \mathcal{U}(10^{-5}, 20)$, and the posteriors from the previous scenario (where the proliferation rate is calibrated) are used as priors for ϕ_{V0} , λ_{apop} , λ_{prol} , and K . The experiments are done with 0%, 2.5%, 5%, and 7.5% of FBS, which are mapped into nutrient volume fractions (ϕ_σ) as 0, 0.25, 0.5, and 0.75, respectively.

In Figure 1c)-f), the calibration of the model, at each nutrient condition, 7.5%, 5%, 2.5%, and 0% of FBS, respectively, is compared with the data from *in vitro* experiments. Using the metric given in Eq. (23), the errors, from the lowest initial condition to the highest, in this scenario 25,000, 50,000, and 100,000 cells/ml, and for the four nutrient concentration, are, respectively, c) 10.70%, 8.12%, and 10.06%; d) 20.87%, 9.93%, and 11.69%; e) 14.14%, 10.85%, and 8.46%; f) 31.55%, 14.90%, and 21.09%. In Figure 5, the necrosis rate, λ_{VN} , for all combinations of initial nutrient and cell concentration are presented. We can observe that λ_{VN} increases as the nutrient available for the cells decreases, and as the initial cell volume fraction increases.

Calibration of tumor cell mobility

In this scenario, the tumor cells spatial distribution is measured, allowing us to calibrate the tumor mobility from the model in Eq. (10). In Figure 6, we present the cancer cells in green over a period of 12 hours with 7.5% of FBS. As we tracked the cells during a short interval, 12 hours, we assume that we can disregard proliferation and apoptosis rates, and assume that necrotic cells are not present, leading to a simplified model:

$$\left. \begin{aligned} \frac{\partial \phi_T}{\partial t} &= \nabla \cdot M_T(\phi) \nabla \mu, \\ \mu &= \Psi'(\phi_T) - \varepsilon_T^2 \Delta \phi_T, \end{aligned} \right\} \quad (27)$$

where the tumor mobility (M_T), the energy scale (E_T), the interaction length (ε_T), and the standard deviation (σ) hyperparameter from Eq. (22) are all calibrated. The calibration priors are assumed to be uniform distributions with $M_T \sim \mathcal{U}(0, 1000)$, $E_T \sim \mathcal{U}(0.15, 1.15)$, $\varepsilon_T \sim \mathcal{U}(1, 1000)$, and $\sigma \sim \mathcal{U}(10^{-5}, 0.2)$, and the posteriors from the previous scenario (where the proliferation rate is calibrated) are used as priors for ϕ_{V0} , λ_{apop} , λ_{prol} , and K . The experiments are done with 0%, 2.5%, 5%, 7.5%, and 10.0% of FBS, and initial cell density of 100,000 cells/ml. In Figure 7, we present the interaction length, ε_T , for the five FBS concentration. The approximated distributions for ε_T , for the five FBS concentrations (i.e., 0%, 2.5%, 5%, 7.5%, and 10.0%), are $\approx \ln \mathcal{N}(4.74, 0.80)$, $\approx \ln \mathcal{N}(3.00, 1.00)$, $\approx \ln \mathcal{N}(2.83, 0.96)$, $\approx \ln \mathcal{N}(3.11, 0.90)$, and $\approx \ln \mathcal{N}(3.18, 1.04)$, respectively. In Figure 8, the mobility rate, M_T , for all initial FBS concentrations are presented.

Discussion

Mathematical models of malignant neoplasms are often developed either as a tool for better understanding of the cancer etiology, that is, understanding the underlying causes of tumor initiation and progression, or as tool for predictive modeling of therapeutic outcomes of cancer treatment. Despite its relatively long history in oncology^{27–29}, development and successful employment of mathematical models of tumor growth in clinical settings are still challenging, largely due to the computational demands of such models, and more importantly, because of the many free parameters of such phenomenological models that often remain poorly constrained, if constrained at all by in-vitro or clinical experiments.

In this work, we used an extensive set of in-vitro experiments to constrain and calibrate the parameters of our proposed phenomenological phase-field model of tumor growth. To calibrate the full phase-field model, we developed a hierarchical experimental design which allowed us to reduce significantly the complexity of the mathematical models to be calibrated. By applying state-of-the-art multilevel Monte Carlo²⁶ and hierarchical Bayesian techniques^{21,30,31}, we were able to optimally constrain the parameters with the experimentally available data.

Simultaneous calibration of model parameters requires complex comprehensive experimental setup that could monitor tumor cell proliferation, viability, apoptosis rate, hypoxia, and mobility all at the same time. This is however impossible given the current available technologies. We therefore brought our calibration problem into the realm of experimental and computational feasibility by constraining and calibrating each parameter separately while fixing the rest of parameters to an experimentally feasible value. One limitation inherent in this approach involves the estimation of the mobility parameter, M_T . We note that when calibrating Eq. (27) to determine tumor cell mobility, we are required to use a shorter time series of microscopy data (approximately 12 hours) so as to isolate observations of mobility from proliferation. However, our expression for the chemical potential, μ (the second equation in (27)), is also determined during the 12 hour time scale. This is a limitation because μ is dependent on ϕ_T which is clearly a function of time; but since ϕ_T is assumed to not change during these 12 hours, our estimation of μ may not be accurate and this may manifest itself as an source of error in the estimation of the mobility. More extensive experiments would be required to further separate these parameters.

The model enables prediction of several unique parameters including proliferation rate, apoptosis rate, necrosis rate, and mobility of liver cancer cells as a function of nutrient concentration and cell seeding density. The parameters and response kinetics obtained from our work could serve as the basis for pharmacokinetic/pharmacodynamics (PK/PD) modeling to measure apoptosis rate after drug treatment. McKenna *et al.* previously showed that the tumor growth and apoptosis rate of breast cancer cells after treatment with doxorubicin at different concentrations and durations, exhibited similar growth trends as presented in Figure 1b)¹³. But, apoptosis and necrosis rates reported by McKenna *et al.* did not demonstrate apoptosis and necrosis rates independent of drug treatment¹³. Apoptosis and necrosis rates without the effect of drug treatment measured in this study enables the differentiation of apoptosis caused by drug and natural cell death. Consequently, the apoptosis and necrosis rates in this study are key parameters for obtaining accurate PK/PD predictions. Also, it is known that cells interact and signal each other when they are proliferating³². Therefore, capturing and modeling cell mobility enables us to predict interaction between cells during proliferation. Moreover, calculated apoptosis results show similarities with previously reported apoptosis rates of HEPG2 liver cancer cells by Sun *et al.*³³. The study conducted Sun *et al.* showed that HEPG2 liver cancer cells showed $7.82 \pm 1.29\%$ per 24 hour apoptosis rate based on their flow cytometry measurements³³, which matches with our finding, $6.67 \pm 0.96\%$ per 24 hours at the same cell concentration. Our proliferation rate of the cancer cells showed variation between 43% and 55% before reaching to plateau-phase. Similarly, Wu *et al.* showed colorectal cancer cells exhibited 38% to 42% proliferation rate³⁴. In fact, cell mobility rate measured in this study was average of $5.12 \mu\text{m}/\text{day}$, which is considered as very low cell mobility. This low mobility was expected since no chemoattractant or stimulant gradients were introduced within our system³⁵. Oppositely, Zervantonakis *et al.* showed HT100 cells were attracted by endothelial cells and cell mobility was measured as $29 \mu\text{m}/\text{hour}$ ³⁶ and Huang *et al.* reported MDA-MB-231 migration through softer tissues as $37 \mu\text{m}/\text{hour}$ ³⁷. For necrosis, Kou *et al.* reported HEPG2 liver cancer cell necrosis rate due to lack of nutrient as 33.87%, which is close to our finding, 29.15%³⁸.

The calibration experiments and results described here are naturally applicable to a specific family of models and to scenarios for which data could be isolated for calibrating specific parameters of the models. Many complexities of the tumor microenvironment were not addressed. The experimental systems used for model calibration consisted of a 2D cell monolayer of liver cancer cells which neglected the 3D extracellular matrix (ECM) effects that can influence cell proliferation rates, cell-matrix interaction, and diffusion of nutrients. As such, key components of the ECM, including porosity, fiber diameter and pore size and common biological phenomena such as matrix stiffening^{39–41} that influence the transport of nutrients and ultimately cell proliferation and migration were not considered. The lack of vasculature in our system discounted the influence of transport and distribution properties such as flow rate and shear stress, which are important for secretion of functional proteins as shown by vascularized *in vitro* study conducted by Ozkan *et al.*⁴⁰. The lack of endothelial cells within the matrix or vasculature eliminates the influence of angiogenesis and cancer-endothelial interaction, which is an important aspect of tumor growth⁴². Furthermore, the lack of stromal cells such as fibroblast in the system limits the influence of ECM remodeling

as the tumor grows and migrates³⁹. When considering cell mobility term in the model, the C3Asub28 cell line used did not exhibit high cell mobility. However, the model has the capability to capture and model cells with more aggressive phenotypes with higher mobility. The model can be easily adapted to account for all the previously mentioned complexities of the tumor microenvironment in parallel with more physiological tumor platforms, to predict cancer growth and response to various therapeutics.

References

1. Byrne, H. M. Dissecting cancer through mathematics: from the cell to the animal model. *Nat. Rev. Cancer* **10**, 221 (2010).
2. Yankeelov, T. E. *et al.* Multi-scale modeling in clinical oncology: opportunities and barriers to success. *Annals biomedical engineering* **44**, 2626–2641 (2016).
3. Oden, J. T. *et al.* Toward Predictive Multiscale Modeling of Vascular Tumor Growth. *Arch. Comput. Methods Eng.* **23**, 735–779 (2016).
4. Rocha, H. L. *et al.* A hybrid three-scale model of tumor growth. *Math. Model. Methods Appl. Sci.* **28**, 61–93 (2018).
5. Hawkins-Daarud, A., van der Zee, K. G. & Oden, J. T. Numerical simulation of a thermodynamically consistent four-species tumor growth model. *Int. J. for Numer. Methods Biomed. Eng.* **28**, 3–24 (2012).
6. Lima, E. A. B. F., Oden, J. T. & Almeida, R. C. A Hybrid Ten-Species Phase-Field Model of Tumor Growth. *Math. Model. Methods Appl. Sci.* **24**, 2569–2599 (2014).
7. Lima, E. A. B. F., Almeida, R. C. & Oden, J. T. Analysis and numerical solution of stochastic phase-field models of tumor growth. *Numer. Methods for Partial. Differ. Equations* **31**, 552–574 (2015).
8. Rahman, M. M., Feng, Y., Yankeelov, T. E. & Oden, J. T. A fully coupled space–time multiscale modeling framework for predicting tumor growth. *Comput. Methods Appl. Mech. Eng.* **320**, 261–286 (2017).
9. Hawkins-Daarud, A., Prudhomme, S., van der Zee, K. G. & Oden, J. T. Bayesian calibration, validation, and uncertainty quantification of diffuse interface models of tumor growth. *J. Math. Biol.* **67**, 1457–1485 (2013).
10. Oden, J. T., Hawkins, A. & Prudhomme, S. General diffuse-interface theories and an approach to predictive tumor growth modeling. *Math. Model. Methods Appl. Sci.* **20**, 477–517 (2010).
11. Oden, J. T., Prudencio, E. E. & Hawkins-Daarud, A. Selection and assessment of phenomenological models of tumor growth. *Math. Model. Methods Appl. Sci.* **23**, 1309–1338 (2013).
12. McKenna, M. T., Weis, J. A., Quaranta, V. & Yankeelov, T. E. Variable cell line pharmacokinetics contribute to non-linear treatment response in heterogeneous cell populations. *Annals biomedical engineering* 1–13 (2018).
13. McKenna, M. T. *et al.* A predictive mathematical modeling approach for the study of doxorubicin treatment in triple negative breast cancer. *Sci. Reports* **7**, 5725 (2017).
14. Waclaw, B. *et al.* A spatial model predicts that dispersal and cell turnover limit intratumour heterogeneity. *Nat.* **525**, 261 (2015).
15. Tyson, D. R., Garbett, S. P., Frick, P. L. & Quaranta, V. Fractional proliferation: a method to deconvolve cell population dynamics from single-cell data. *Nat. methods* **9**, 923 (2012).
16. Lima, E. A. B. F., Oden, J. T., Hormuth II, D. A., Yankeelov, T. E. & Almeida, R. C. Selection, calibration, and validation of models of tumor growth. *Math. Model. Methods Appl. Sci.* **26**, 2341–2368 (2016).
17. Lima, E. A. B. F. *et al.* Selection and validation of predictive models of radiation effects on tumor growth based on noninvasive imaging data. *Comput. Methods Appl. Mech. Eng.* **327**, 277–305 (2017).
18. Cristini, V., Li, X., Lowengrub, J. S. & Wise, S. M. Nonlinear simulations of solid tumor growth using a mixture model: invasion and branching. *J. mathematical biology* **58**, 723–763 (2009).
19. Wise, S. M., Lowengrub, J. S., Frieboes, H. B. & Cristini, V. Three-dimensional multispecies nonlinear tumor growth—i: model and numerical method. *J. theoretical biology* **253**, 524–543 (2008).
20. Eyre, D. J. Unconditionally gradient stable time marching the cahn-hilliard equation. *MRS Online Proc. Libr. Arch.* **529** (1998).
21. Shahmoradi, A. Multilevel bayesian parameter estimation in the presence of model inadequacy and data uncertainty. *arXiv preprint arXiv:1711.10599* (2017).

22. Prudencio, E. & Cheung, S. H. Parallel adaptive multilevel sampling algorithms for the Bayesian analysis of mathematical models. *Int. J. for Uncertain. Quantification* **2**, 215–237 (2012).
23. Tae-im Kim, S.-i. C., Lee, H. K., Cho, Y. J. & Kim, E. K. Mitomycin c induces apoptosis in cultured corneal fibroblasts derived from type ii granular corneal dystrophy corneas. *Mol. vision* **14**, 1222 (2008).
24. Wu, K.-Y., Wang, H.-Z. & Hong, S.-J. Mechanism of mitomycin-induced apoptosis in cultured corneal endothelial cells. *Mol. vision* **14**, 1705 (2008).
25. Kirk, B. S., Peterson, J. W., Stogner, R. H. & Carey, G. F. libMesh: A C++ Library for Parallel Adaptive Mesh Refinement/Coarsening Simulations. *Eng. with Comput.* **22**, 237–254 (2006).
26. Prudencio, E. E. & Schulz, K. W. The Parallel C++ Statistical Library 'QUESO': Quantification of Uncertainty for Estimation, Simulation and Optimization. In Alexander, M. *et al.* (eds.) *Euro-Par 2011: Parallel Processing Workshops*, vol. 7155 of *Lecture Notes in Computer Science*, 398–407 (Springer Berlin Heidelberg, 2012).
27. Thomlinson, R. & Gray, L. The histological structure of some human lung cancers and the possible implications for radiotherapy. *Br. journal cancer* **9**, 539 (1955).
28. Burton, A. C. Rate of growth of solid tumours as a problem of diffusion. *Growth* **30**, 157–176 (1966).
29. Iyer, K. & Saksena, V. A stochastic model for the growth of cells in cancer. *Biom.* 401–410 (1970).
30. Oden, J., Babuska, I. & Faghihi, D. Predictive computational science: Computer predictions in the presence of uncertainty. *Encycl. Comput. Mech. E. Stein, R. de Borst, TJR Hughes, eds., Wiley, Hoboken, NJ* (2004).
31. Oden, J. T. Adaptive multiscale predictive modelling. *Acta Numer.* **27**, 353–450 (2018).
32. Mason, E. F. & Rathmell, J. C. Cell metabolism: an essential link between cell growth and apoptosis. *Biochimica et Biophys. Acta (BBA)-Molecular Cell Res.* **1813**, 645–654 (2011).
33. Jia, K. *et al.* Activated δ -opioid receptors inhibit hydrogen peroxide-induced apoptosis in liver cancer cells through the pkc/erk signaling pathway. *Mol. medicine reports* **10**, 839–847 (2014).
34. Wu, R. *et al.* Effects of cd73 on human colorectal cancer cell growth in vivo and in vitro. *Oncol. reports* **35**, 1750–1756 (2016).
35. Paul, C. D., Mistriotis, P. & Konstantopoulos, K. Cancer cell motility: lessons from migration in confined spaces. *Nat. Rev. Cancer* **17**, 131 (2017).
36. Zervantonakis, I. K. *et al.* Three-dimensional microfluidic model for tumor cell intravasation and endothelial barrier function. *Proc. Natl. Acad. Sci.* **109**, 13515–13520 (2012).
37. Huang, Y.-T., Lan, Q., Lorusso, G., Duffey, N. & Rüegg, C. The matricellular protein cyr61 promotes breast cancer lung metastasis by facilitating tumor cell extravasation and suppressing anoikis. *Oncotarget* **8**, 9200 (2017).
38. Kou, X. *et al.* Tumor necrosis factor- α attenuates starvation-induced apoptosis through upregulation of ferritin heavy chain in hepatocellular carcinoma cells. *BMC cancer* **13**, 438 (2013).
39. Buchanan, C. F. *et al.* Three-dimensional microfluidic collagen hydrogels for investigating flow-mediated tumor-endothelial signaling and vascular organization. *Tissue Eng. Part C: Methods* **20**, 64–75 (2013).
40. Ozkan, A., Ghousifam, N. & Rylander, M. N. *In Vitro* vascularized liver and tumor tissue microenvironments on a chip for dynamic determination of nanoparticle transport. *submitted to Lab-on-a-Chip* (2018).
41. Antoine, E., Vlachos, P. & Rylander, M. N. Tunable collagen I hydrogels for engineered physiological tissue microenvironments. *PloS one* **10**, e0122500 (2014).
42. Szot, C. S., Buchanan, C. F., Freeman, J. W. & Rylander, M. N. 3d in vitro bioengineered tumors based on collagen i hydrogels. *Biomater.* **32**, 7905–7912 (2011).

Acknowledgements

The authors acknowledge the support of the Cancer Prevention Research Institute of Texas (CPRIT) for funding part of this work through grant RR160005, the NCI for funding through grants U01CA174706, and R01CA186193, the U.S. Department of Energy Office of Science, Office of Advanced Scientific Computing Research, Applied Mathematics program under Award Number DE-5C0009286, and the German Science Foundation (DFG, WO-671 11-1).

Parameter	Initial condition (1,000 cells/ml)				
	5	10	25	50	100
λ_{apop} (day ⁻¹)	$\mathcal{N}(0.06, 0.02)$	$\mathcal{N}(0.06, 0.02)$	$\mathcal{N}(0.09, 0.03)$	$\mathcal{N}(0.09, 0.02)$	$\mathcal{N}(0.11, 0.02)$
λ_{prol} (day ⁻¹)	$\mathcal{N}(0.43, 0.02)$	$\mathcal{N}(0.48, 0.02)$	$\mathcal{N}(0.55, 0.05)$	$\mathcal{N}(0.55, 0.05)$	$\ln \mathcal{N}(0.43, 0.64)$
K (dimensionless)	$\mathcal{N}(0.13, 0.01)$	$\mathcal{N}(0.13, 0.01)$	$\mathcal{N}(0.14, 0.01)$	$\mathcal{N}(0.14, 0.01)$	$\mathcal{N}(0.12, 0.01)$
λ_{VN} (day ⁻¹) (7.5% FBS)	n/a	n/a	$\ln \mathcal{N}(-3.57, 1.14)$	$\ln \mathcal{N}(-5.13, 1.18)$	$\ln \mathcal{N}(-6.27, 1.41)$
λ_{VN} (day ⁻¹) (5.0% FBS)	n/a	n/a	$\ln \mathcal{N}(-3.07, 1.05)$	$\ln \mathcal{N}(-5.05, 1.17)$	$\ln \mathcal{N}(-5.60, 1.25)$
λ_{VN} (day ⁻¹) (2.5% FBS)	n/a	n/a	$\mathcal{N}(0.18, 0.08)$	$\ln \mathcal{N}(-4.27, 1.07)$	$\ln \mathcal{N}(-5.05, 1.15)$
λ_{VN} (day ⁻¹) (0.0% FBS)	n/a	n/a	$\ln \mathcal{N}(-4.36, 1.42)$	$\mathcal{N}(0.08, 0.02)$	$\mathcal{N}(0.09, 0.02)$
ε_T (μm) (10.0% FBS)	n/a	n/a	n/a	n/a	$\ln \mathcal{N}(3.18, 1.04)$
ε_T (μm) (7.5% FBS)	n/a	n/a	n/a	n/a	$\ln \mathcal{N}(3.11, 0.90)$
ε_T (μm) (5.0% FBS)	n/a	n/a	n/a	n/a	$\ln \mathcal{N}(2.83, 0.96)$
ε_T (μm) (2.5% FBS)	n/a	n/a	n/a	n/a	$\ln \mathcal{N}(3.00, 1.00)$
ε_T (μm) (0.0% FBS)	n/a	n/a	n/a	n/a	$\ln \mathcal{N}(4.74, 0.80)$
M_T ($\mu\text{m}/\text{day}$) (10.0% FBS)	n/a	n/a	n/a	n/a	$\ln \mathcal{N}(5.23, 1.62)$
M_T ($\mu\text{m}/\text{day}$) (7.5% FBS)	n/a	n/a	n/a	n/a	$\ln \mathcal{N}(5.32, 1.57)$
M_T ($\mu\text{m}/\text{day}$) (5.0% FBS)	n/a	n/a	n/a	n/a	$\ln \mathcal{N}(4.96, 1.67)$
M_T ($\mu\text{m}/\text{day}$) (2.5% FBS)	n/a	n/a	n/a	n/a	$\ln \mathcal{N}(4.50, 1.74)$
M_T ($\mu\text{m}/\text{day}$) (0.0% FBS)	n/a	n/a	n/a	n/a	$\ln \mathcal{N}(5.20, 1.49)$

Table 1. Fitted distributions for the calibrated parameters under different initial and FBS conditions.

List of Figures

1	Mean volume fraction and credible interval of viable tumor cells for up to five different initial cell concentration: 100,000, 50,000, 25,000, 10,000, and 5,000 cells/ml. The solid lines represent the calibrated model. (a) Aiming to stop proliferation and be able to observe apoptosis, the cells are treated with 10 $\mu\text{g/ml}$ of Mitomycin-C for two hours. The average calibration error, for each initial condition, is between 11.54% and 14.04%. (b) Cells without Mitomycin-C with serum concentration of 10%, measured every day, during 21 days, to calibrate the proliferation of the tumor. After an initial growth phase, the cells reach the carrying capacity. The average calibration error, for each initial condition, is between 7.33% and 23.30%. (c)-(f) Evolution of the tumor for different supplies of serum concentration (nutrient), respectively, 7.5%, 5%, 2.5% and 0%. The maximum volume fraction decreases as the initial nutrient is reduced. The average calibration error, for each initial condition, is between 8.12% and 31.55%, with the highest error for the 25,000 cells/ml in f).	14
2	Histogram of the apoptosis rate and the fitted probability density function (PDF) for five different initial conditions treated with Mitomycin-C at a concentration of 10 $\mu\text{g/ml}$ for two hours. The apoptosis rate is proportional to the initial concentration of cells, with the 5,000 and 10,000 cells/ml having the lowest, the 25,000 and 50,000 cells/ml the intermediate, and the 100,000 cells/ml the highest apoptosis rate.	15
3	(a) Posterior pdf of the apoptosis rate obtained through the calibration of the data with Mitomycin-C. This pdf is used as a prior during the calibration of the proliferation rate for the data without Mitomycin-C. (b) Posterior pdf of the apoptosis rate computed during the calibration of the data without Mitomycin-C. The difference between the prior and posterior on the calibration of the apoptosis rate, from the lowest initial condition (5,000 cells/ml) to the highest (100,000 cells/ml), is 0.42%, 3.09%, 1.40%, 0.46%, and 4.38%, respectively.	16
4	Histogram of the proliferation rate, λ_{prol} , and the fitted probability density function (PDF) for five different initial conditions. The proliferation rate is proportional to the initial concentration of cells. As the initial condition of the 100,000 cells/ml is close to the carrying capacity, the proliferation rate doesn't affects the tumor growth after day 3, leading to a wider range on the distribution of λ_{prol}	17
5	Histogram of the necrosis rate, λ_{VN} , for four FBS concentration, from top to bottom, 7.5%, 5.0%, 2.5%, and 0.0%, respectively, and three initial conditions, from left to right, 25,000, 50,000, and 100,000 cells/ml. The necrosis rate increases as the FBS concentration decreases and the number of initial cells increases.	18
6	Spatial distribution of liver cancer cells over time. Cells were transfected with green fluorescent protein.	19
7	Histogram of the interaction length, ϵ_T , for five FBS concentration: 0.0%, 2.5%, 5.0%, 7.5%, and 10.0%, and the same initial cell density of 100,000 cells/ml.	20
8	Histogram of the mobility rate, M_T , for five FBS concentration: 0.0%, 2.5%, 5.0%, 7.5%, and 10.0%, and the same initial cell density of 100,000 cells/ml.	21

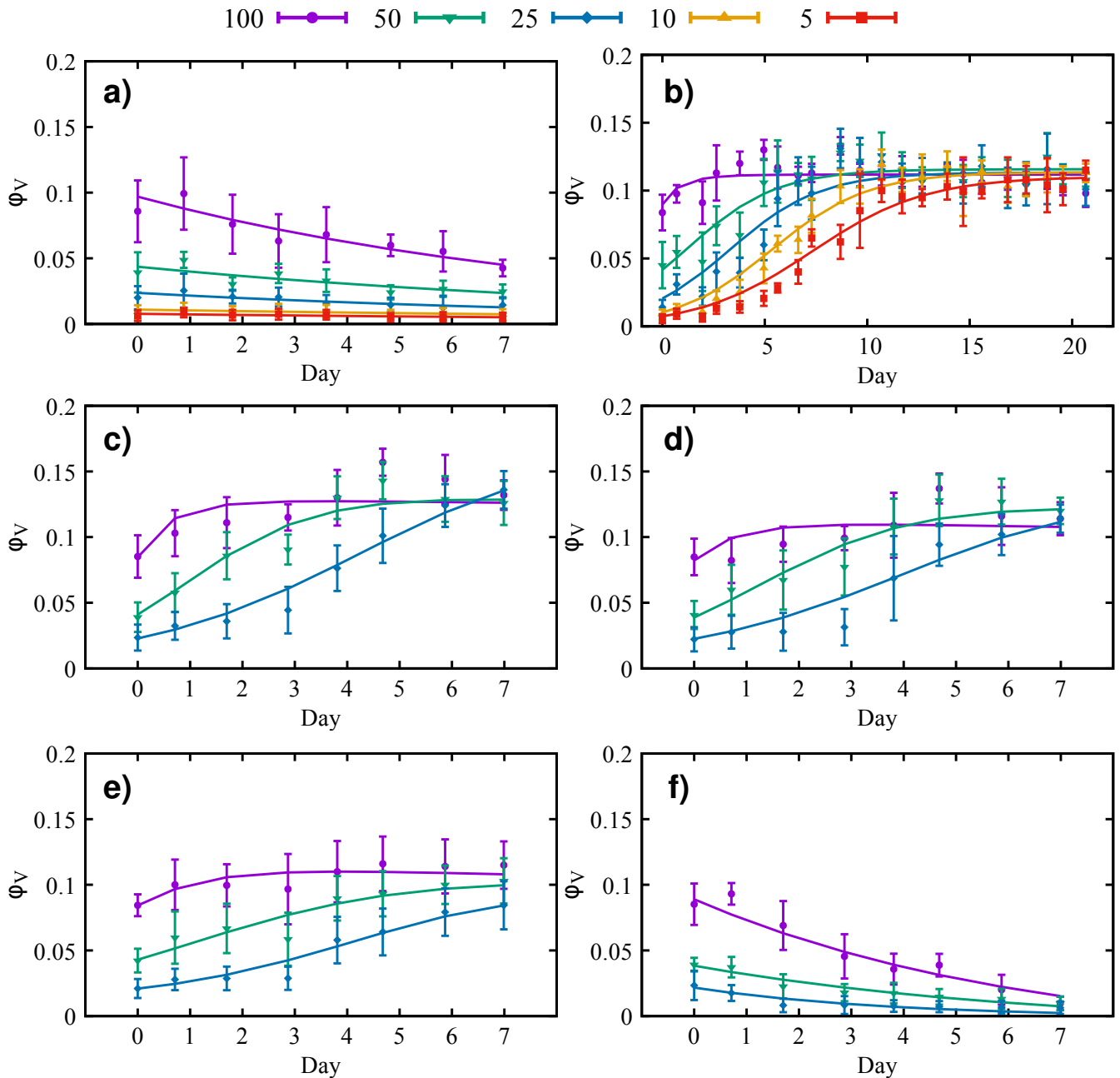


Figure 1. Mean volume fraction and credible interval of viable tumor cells for up to five different initial cell concentration: 100,000, 50,000, 25,000, 10,000, and 5,000 cells/ml. The solid lines represent the calibrated model. (a) Aiming to stop proliferation and be able to observe apoptosis, the cells are treated with 10 $\mu\text{g/ml}$ of Mitomycin-C for two hours. The average calibration error, for each initial condition, is between 11.54% and 14.04%. (b) Cells without Mitomycin-C with serum concentration of 10%, measured every day, during 21 days, to calibrate the proliferation of the tumor. After an initial growth phase, the cells reach the carrying capacity. The average calibration error, for each initial condition, is between 7.33% and 23.30%. (c)-(f) Evolution of the tumor for different supplies of serum concentration (nutrient), respectively, 7.5%, 5%, 2.5% and 0%. The maximum volume fraction decreases as the initial nutrient is reduced. The average calibration error, for each initial condition, is between 8.12% and 31.55%, with the highest error for the 25,000 cells/ml in f).

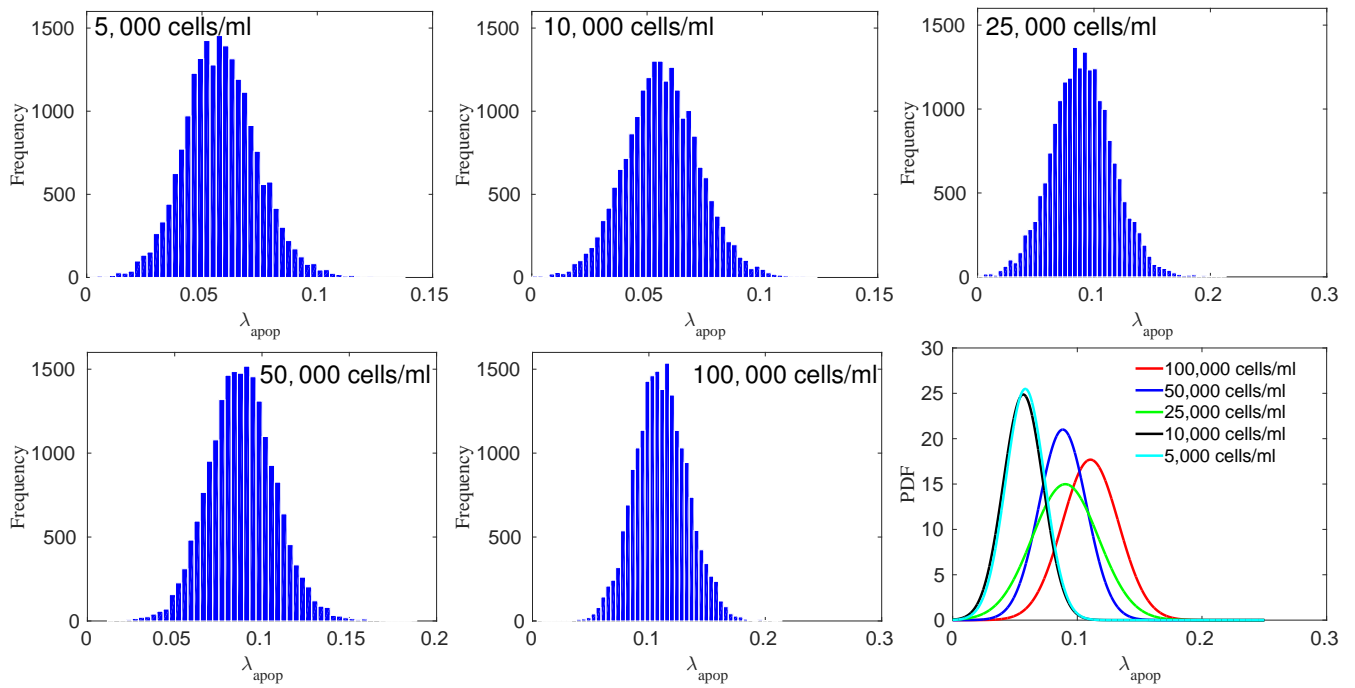


Figure 2. Histogram of the apoptosis rate and the fitted probability density function (PDF) for five different initial conditions treated with Mitomycin-C at a concentration of $10 \mu\text{g/ml}$ for two hours. The apoptosis rate is proportional to the initial concentration of cells, with the 5,000 and 10,000 cells/ml having the lowest, the 25,000 and 50,000 cells/ml the intermediate, and the 100,000 cells/ml the highest apoptosis rate.

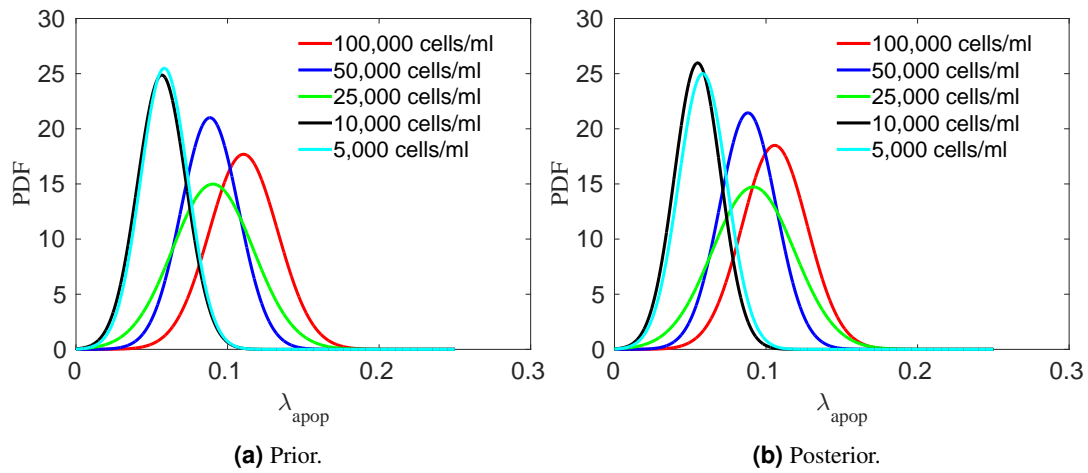


Figure 3. (a) Posterior pdf of the apoptosis rate obtained through the calibration of the data with Mitomycin-C. This pdf is used as a prior during the calibration of the proliferation rate for the data without Mitomycin-C. (b) Posterior pdf of the apoptosis rate computed during the calibration of the data without Mitomycin-C. The difference between the prior and posterior on the calibration of the apoptosis rate, from the lowest initial condition (5,000 cells/ml) to the highest (100,000 cells/ml), is 0.42%, 3.09%, 1.40%, 0.46%, and 4.38%, respectively.

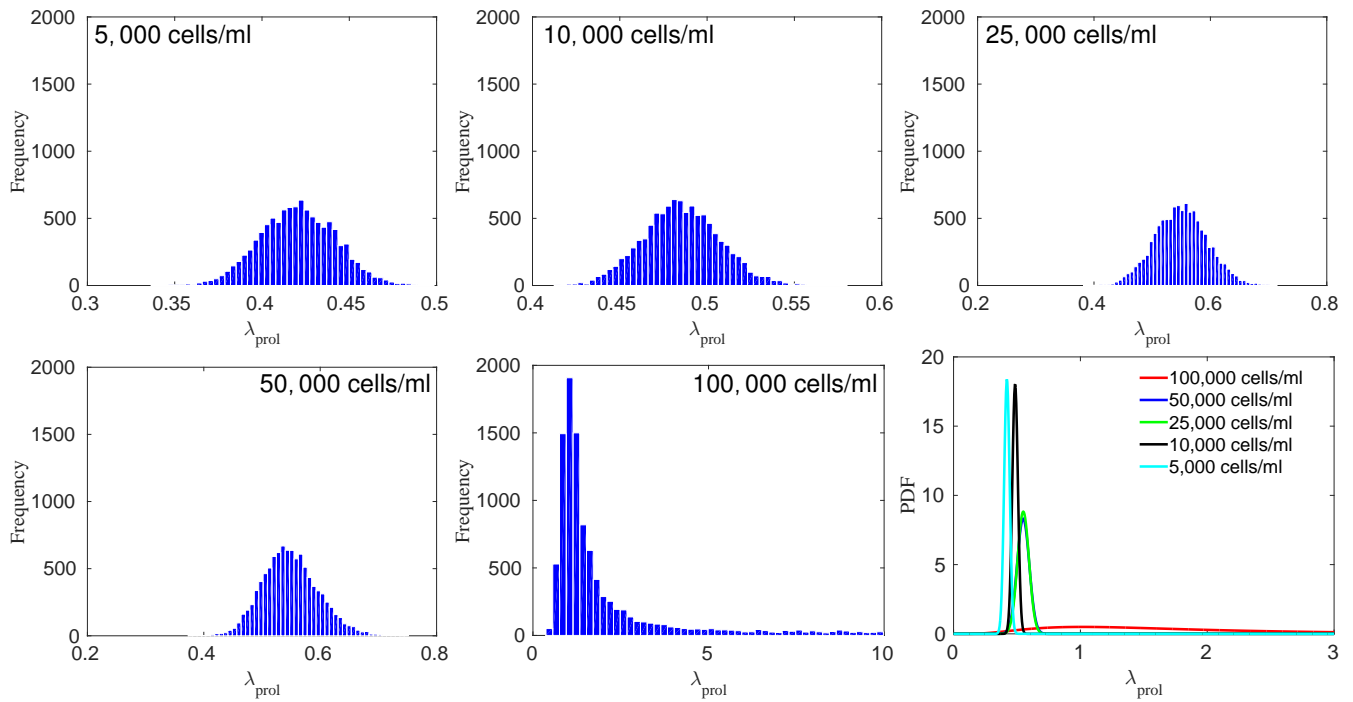


Figure 4. Histogram of the proliferation rate, λ_{prol} , and the fitted probability density function (PDF) for five different initial conditions. The proliferation rate is proportional to the initial concentration of cells. As the initial condition of the 100,000 cells/ml is close to the carrying capacity, the proliferation rate doesn't affect the tumor growth after day 3, leading to a wider range on the distribution of λ_{prol} .

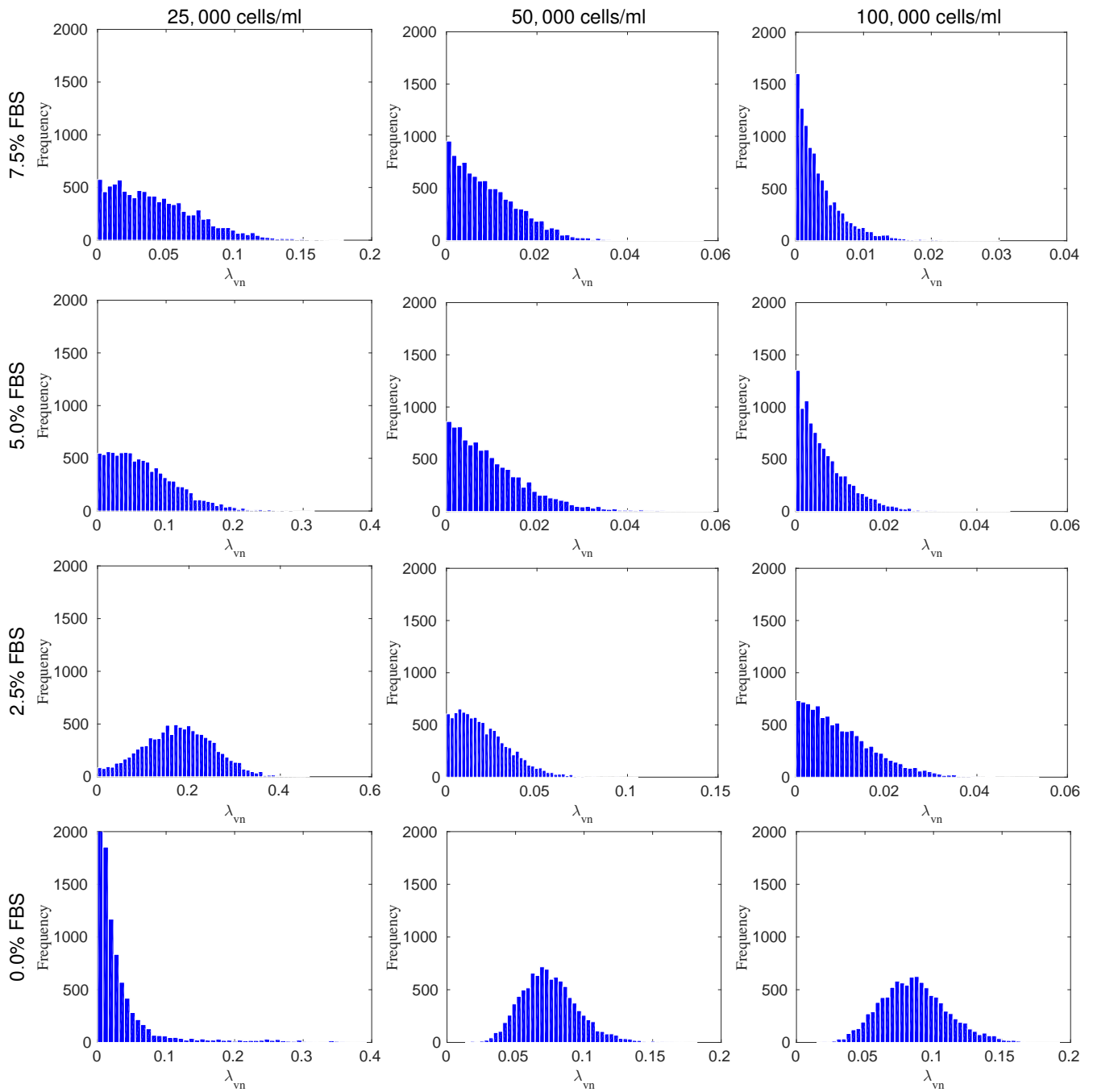


Figure 5. Histogram of the necrosis rate, λ_{vN} , for four FBS concentration, from top to bottom, 7.5%, 5.0%, 2.5%, and 0.0%, respectively, and three initial conditions, from left to right, 25,000, 50,000, and 100,000 cells/ml. The necrosis rate increases as the FBS concentration decreases and the number of initial cells increases.

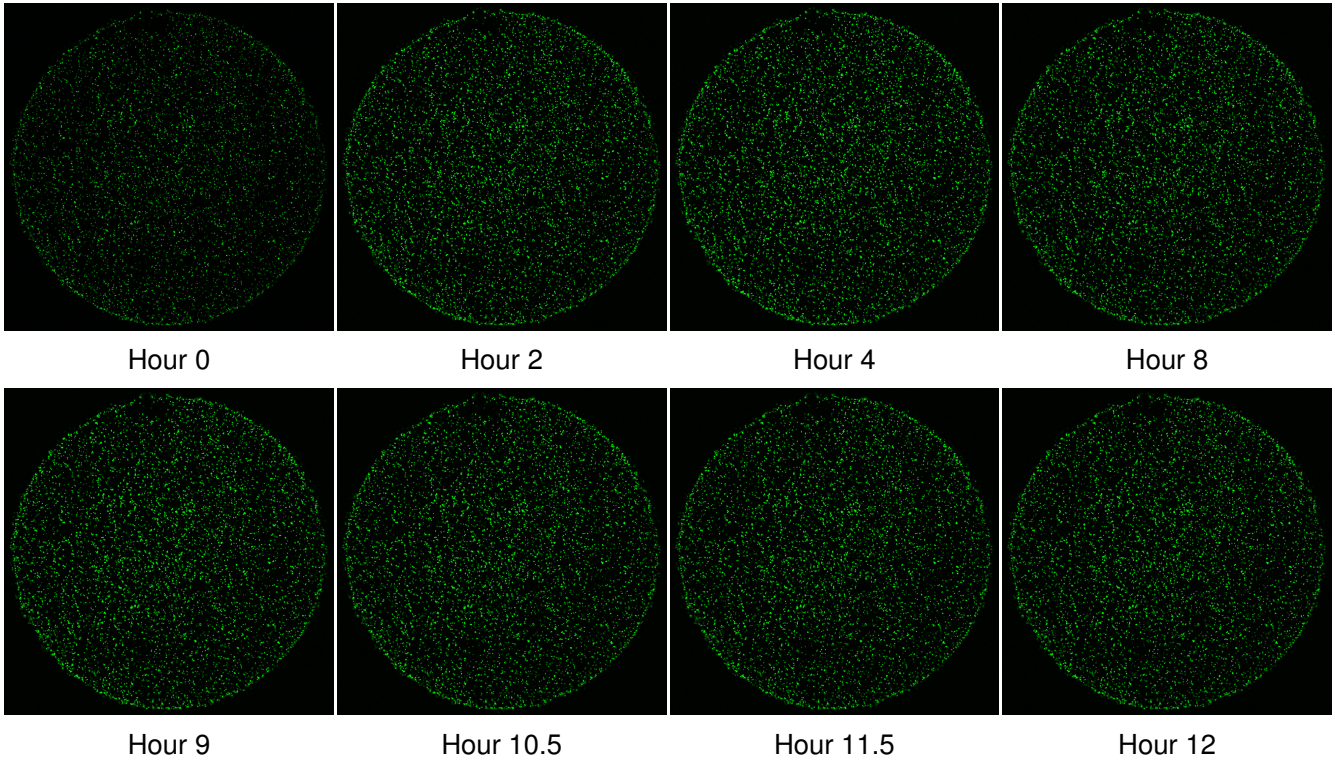


Figure 6. Spatial distribution of liver cancer cells over time. Cells were transfected with green fluorescent protein.

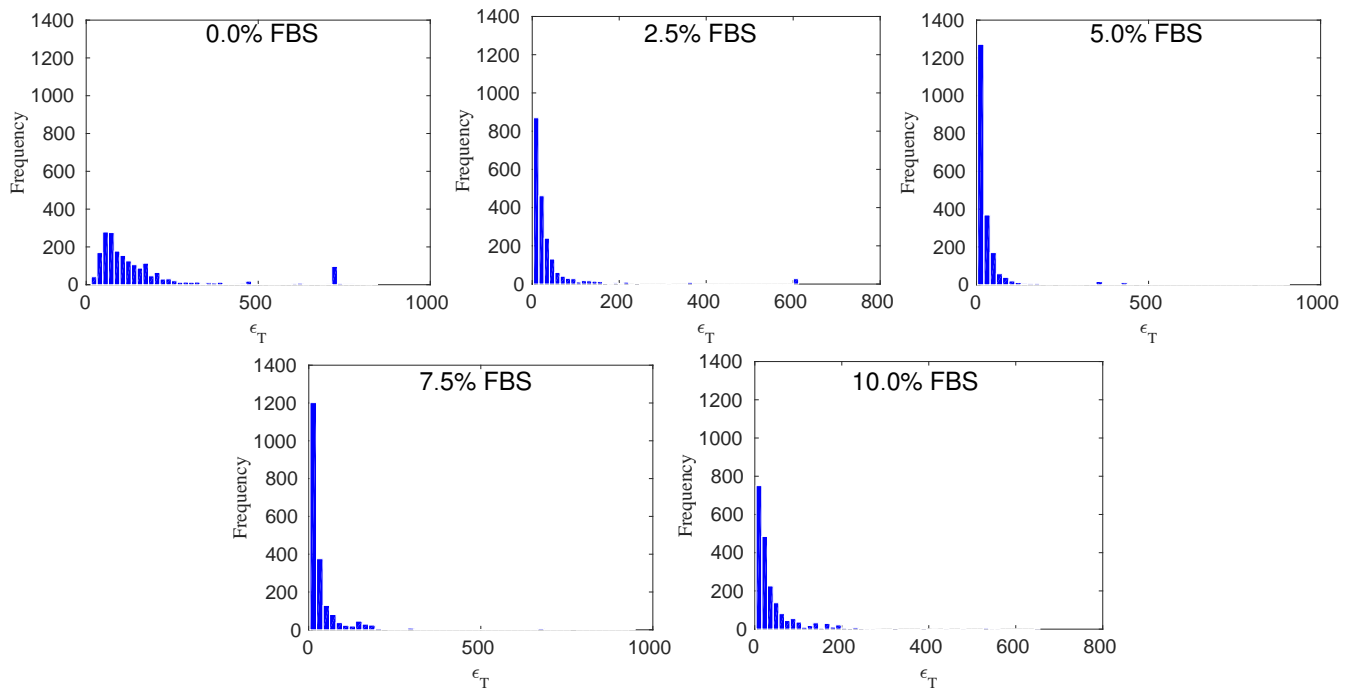


Figure 7. Histogram of the interaction length, ϵ_T , for five FBS concentration: 0.0%, 2.5%, 5.0%, 7.5%, and 10.0%, and the same initial cell density of 100,000 cells/ml.

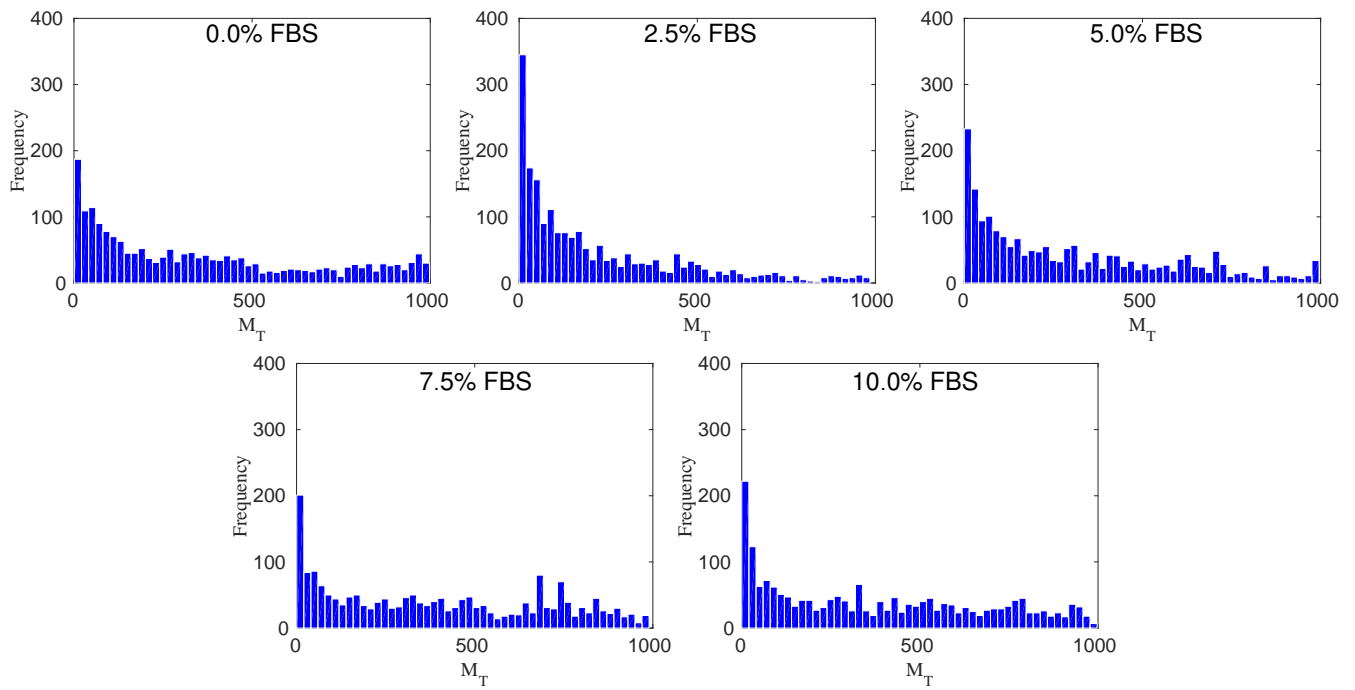


Figure 8. Histogram of the mobility rate, M_T , for five FBS concentration: 0.0%, 2.5%, 5.0%, 7.5%, and 10.0%, and the same initial cell density of 100,000 cells/ml.